EVALUATING THE PERFORMANCE OF DISTRIBUTED ACOUSTIC SENSING FOR CROSSWELL SEISMIC IMAGING OF ABANDONED MINE GEOTHERMAL SYSTEMS

Joanna M. Holmgren[1,2], Antony Butcher[1], Maximilian J. Werner[1], Sacha Lapins[1], Jonathan Chambers[3], J-Michael Kendall[4], Germán Rodríguez[1], James Verdon[1], and Vanessa Starcher[3]

1) School of Earth Sciences, University of Bristol, Queens Road, Bristol, BS8 1RJ, UK
2) NORSAR, Kjeller, Norway
3) British Geological Survey, Keyworth, UK
4) Department of Earth Sciences, University of Oxford, South Parks Road, Oxford OX1 3AN, UK

Corresponding author: Joanna M. Holmgren, School of Earth Sciences, University of Bristol, Queens Road, Bristol, BS8 1RJ, UK. *Now at:* NORSAR, Gunnar Randers vei 15, N-2027 Kjeller, Norway. joanna.holmgren@norsar.no

Original paper date of submission: 16 August 2024

Accepted for publication date: 04 April 2025

Abstract

We explore the performance of Distributed Acoustic Sensing (DAS) for crosswell seismic imaging at a shallow geothermal project in an abandoned mine. The UK Geoenergy Observatory (UKGEOS) research facility in Glasgow has repurposed an abandoned coal mine below the city with the goal to investigate the heat storage and heat recovery potential of flooded mines. Originally for distributed temperature sensing purposes, UKGEOS installed fiber-optic cables in <100 m deep boreholes passing through the mined coal seams now targeted for heat production. We first conducted a crosswell active-source seismic survey prior to heat pump installation to obtain a baseline velocity structure of the coal seams and surrounding lithologies. We acquired data simultaneously with DAS and a co-located hydrophone array to facilitate a comparison with conventional crosswell methods. We find that the noise levels are significantly higher for DAS, making first arrivals discernible only within 30 m vertical offset between shot and channel depths which limits the DAS monitoring depth range along the borehole. However, the DAS coda provides much greater spatial resolution that can capture refracted arrivals, allowing for accurate and precise identification of discrete layers. Future repeated surveys with DAS can thus shed important light on any changes within the seismic velocity structure between the boreholes, indicating potential changes in fracture zones and fluid pathways. As repurposing abandoned coal mines for geothermal energy has been shown to be a promising alterative geoenergy source, DAS could be an inexpensive and simpler alternative to drilling monitoring wells and deploying conventional seismic arrays.

Introduction

Disused mines that have flooded since their abandonment represent a promising but untapped geoenergy source (e.g., Hall et al., 2011; Verhoeven et al., 2014; Adams et al., 2019; Dobson et al., 2023). Considering the large number of UK cities and towns located above flooded abandoned mines (Adams et al., 2019; Farr et al., 2021), tapping into these renewable resources could significantly aid in the decarbonization of domestic and commercial heating. During the development of mine water geothermal projects, subsurface characterization is needed to accurately determine the size of the potential resource, to optimize the design of heat extraction facilities, and to identify any potential subsurface impacts and environmental hazards. For such cases, geophysical measurements prior to operations are invaluable to provide a baseline against which changes caused by geothermal operations, such as alterations in fluid pathways or fracture networks (e.g., Furre et al., 2017; Koedel et al., 2024), can be accurately identified. Furthermore, there is also a need to develop a greater understanding of how different geophysical methods can be used to better constrain the potential geothermal resource in these shallow, urban settings.

In an effort to investigate the heat storage and heat recovery potential of abandoned mines, the UK Geoenergy Observatory (UKGEOS) in Glasgow has repurposed a flooded coal mine beneath the city into a research facility (Monaghan et al., 2022). The shallow geothermal site takes advantage of the warm water (12-20°C) that has filled the mine at ~100 m depth (Watson et al., 2019), and targets two coal seams (but intersects three) within the Scottish Coal Measures that were mined between 1805 and 1928 (Figure 1). The facility comprises of three different sub-sites of mine water boreholes drilled to depths ranging between 52 to 92 m, each installed with permanent fiber-optic cables and providing an excellent opportunity to assess the capabilities of Distributed Acoustic Sensing (DAS) for subsurface characterization.

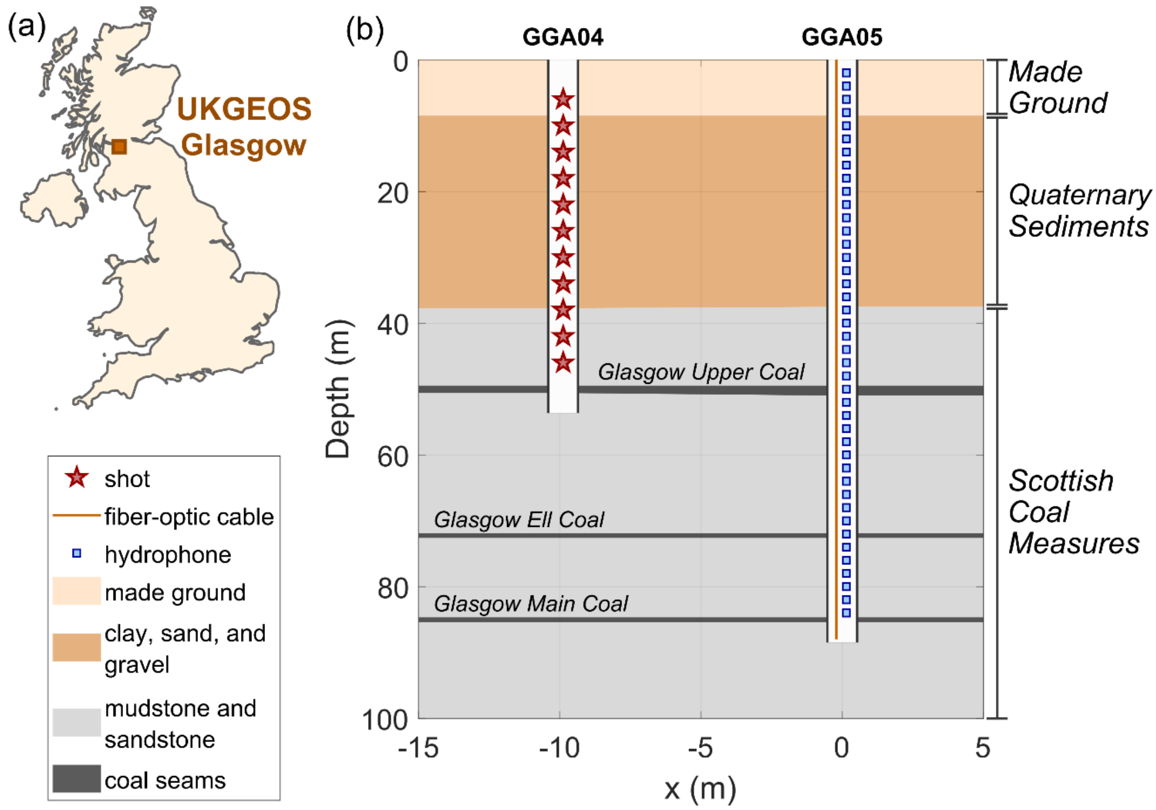

Figure 1. (a) Map of United Kingdom with the UKGEOS Glasgow research facility highlighted. (b) UKGEOS' Site 2 overview with boreholes GGA04 and GGA05, survey shot locations, survey receiver locations, and main surrounding lithology (Barron et al., 2020; Starcher et al., 2020). Note, there is also a permanent fiber-optic cable in GGA04 which was not used during the survey.

DAS has evolved into a powerful seismic acquisition method utilizing fiber-optic cables to measure acoustic and seismic vibrations (e.g., Baird et al., 2020; Lellouch et al., 2020; Lellouch and Biondi 2021). The technique is based on measuring the change in backscattered light along a fiber-optic cable, providing a measure of the change in strain caused by e.g., small temperature variations, seismic vibrations, or static geomechanical deformation. DAS acquisition provides higher spatial resolution than conventional surveys, enabling the full seismic wavefield, including reflected and refracted arrivals, to be examined in greater detail. Moreover, fiber-optic cables can be placed behind borehole casing during well completion, such that data can be acquired without the need to have a dedicated monitoring well. In contrast, hydrophones will fully occupy a borehole and prevent its use for other purposes or require that the instruments are repeatedly inserted and removed from the borehole. As a seismic acquisition method, DAS has been successfully used for seismic monitoring of longwall coal mining (e.g., Tourei et al., 2024). Similarly, DAS monitoring has been successfully applied in fluid-injection settings such as deep enhanced geothermal production (e.g., Lellouch et al., 2020) and hydraulic fracturing (e.g., Verdon et al., 2020). However, these settings are a few kilometers deep within the subsurface and hence the noise levels are lower. In general, DAS acquisition tends to have higher noise levels than conventional instruments (e.g., Correa et al., 2017; Shao et al., 2022), and thus its suitability for urban, shallow mine geothermal systems needs to be investigated.

In this study, we first describe our crosswell seismic survey at Glasgow Observatory to obtain a geophysical baseline measurement of the coal seams and surrounding strata before the heat pump installation commenced at the beginning of February 2022. Alongside the preinstalled fiber-optic cables, we acquired a more conventional seismic data set with co-located hydrophones. Next, we assess the data quality of the two different acquisition techniques by comparing their noise levels and first phase arrival clarity and compute a baseline velocity structure using seismic crosswell tomography. Finally, we investigate if further information can be extracted from reflected and refracted phases in the coda of the DAS data.

Seismic Survey and Dataset Description

To perform our DAS noise and baseline analysis, we use DAS and hydrophone data collected during a crosswell seismic monitoring survey completed in January-February 2022 at the

UKGEOS Glasgow research facility. The survey was carried out at the facility's Site 2 using two boreholes, GGA04 and GGA05, which were 10 m apart and drilled to depths of 53 and 88 m, respectively. Figure 1b shows the depth of the boreholes and the surrounding lithology based on rock chip logs (Barron et al., 2020; Starcher et al., 2020). The top 8-10 m are composed of made ground, consisting of deposits from the industrial past of the area. The made ground overlays a layer of Quaternary deposits roughly 30 m thick containing layers of clay, sand, and gravel. These layers rest upon the 300-m thick Scottish Coal Measures Group, consisting of mudstone, sandstone, and seams of coal. Three coal seams can be found within the borehole depths: Glasgow Upper Coal at 50 m depth with mainly intact or collapsed coal, Glasgow Ell Coal at 72 m depth consisting of very densely packed backfilled mine waste, and Glasgow Main Coal at 85 m depth which has been fully worked and is a water filled void (Monaghan et al., 2022). Borehole GGA04 extends down to the top coal seam Glasgow Upper Coal, while GGA05 was drilled through the deeper coal seams Glasgow Ell Coal and Glasgow Main Coal. Each borehole contains two loops of permanently installed linear, multimode fiber-optic cables between the innermost plastic borehole casing and the cement, originally installed for distributed temperature sensing purposes. Considering that DAS is optimized for single-mode cables, relying on multimode may lead to higher noise levels. Furthermore, there was ongoing construction work taking place nearby during the survey, further increasing the noise levels in this urban setting.

For the active seismic survey, borehole GGA05 was used as the receiver borehole because of its greater depth span. One of its fiber-optic cable loops was connected to a Silixa DAS interrogator (iDAS) and recorded using parameters optimized for a near-surface, short-distance crosswell survey: sampling rate of 10 kHz, 0.25-m channel spacing, and 3-m gauge length. Additionally, a Geomatrix DHA-7 24-channel hydrophone array was deployed inside the borehole and recorded with a sampling rate of 8 kHz and 2-m channel spacing using a Geomatrix Geode seismograph. GGA04 acted as the source borehole, into which a Geotomographie SGS42 Sparker Probe was lowered and connected to an Impulse Generator (IPG) 5000 Downhole Sparker to generate P-waves, delivering short electrical impulses of energy (up to 1000 Joules) at 4 kHz. The receiver and shot locations are shown in Figure 1b. During the survey, 11 shot depths were used, setting off the P-wave sparker in 4-m intervals between 6- and 46-m depth. Because the hydrophone array was 46 m long, covering only half of the GGA05 borehole, the survey was carried out twice with the hydrophones first deployed in the bottom half of GGA05 and then raised to cover the top half. In total, the source was set off 6-7 times at each shot depth, allowing for stacking to enhance the signal content of both the collected DAS and hydrophone data.

Signal and Noise Analysis

DAS data are known to have higher noise levels compared to conventional seismic sensors (e.g., Correa et al., 2017; Shao et al., 2022). This is partly due to DAS being sensitive to strain changes along the direction of the fiber, thus essentially blind to any P-waves arriving perpendicular to the cable. Additionally, DAS is sensitive to several other factors such as the coupling of the cable to the borehole, layout, and instrument noise. To evaluate the limitations and strengths of DAS as a seismic monitoring technique in an urban, shallow geothermal setting, we compare the DAS and hydrophone data from the crosswell active survey.

As expected, the active shots are hardly seen in the raw DAS strain-rate data due to the noisy urban setting and the additional high noise levels caused by nearby construction activity (Supporting Information Figure S1). In contrast, the hydrophone data produced visible first arrivals without any pre-processing required. To enhance the DAS signal, we assess three different denoising approaches. The first approach involves simply stacking the raw DAS data with common shot depths. Moreover, because the DAS data were recorded on a looped fiber-optic cable, the downgoing and upgoing cables are also stacked to further improve the signal. In the second denoising approach, we band-pass filtered the DAS traces between 100 Hz and 1000 Hz before stacking, which corresponds to the attenuated source's main frequency content. We also tried frequency-wavenumber (F-K) filtering, however, we did not find that this made any significant improvement to the signal strength. For the third denoising approach, we apply a weakly supervised machine learning method for fully automated random noise suppression in DAS data called DAS-N2N (Lapins et al., 2024). We use the pre-trained model from Lapins et al. (2024), which was developed to enhance coherent seismic signals using a data set from a DAS array deployed on the surface of the Rutford Ice Stream in Antarctica (Hudson et al., 2021). For DAS-N2N, two noisy copies of the same underlying signal are obtained by splicing two fibers within the same optical cable, each corrupted by independent realizations of random noise. A model is then trained to predict a denoised copy of the signal using only these noisy observations without the need for manually labeled data, providing a hands-off approach for removing strong incoherent noise in DAS data.

The results for the three denoising approaches can be seen in Figure 2 for the shot depth at 34 m, along with the stacked hydrophone traces (unfiltered) and first-arrival picks for the hydrophones. While the raw stacked DAS traces enhance the signal enough to distinguish it from the background noise (Figure 2a), the main features are still difficult to discern due to the high noise levels. In contrast, both the band-pass filter and DAS-N2N approaches are able to enhance the first arrivals and additional features within the coda.

When comparing the two denoising approaches, the pre-trained DAS-N2N model suppresses the background noise slightly better, while at the same time preserving the full frequency spectrum of the source. See Supporting Information Figures S2-S12 for denoising of all the shot depths.

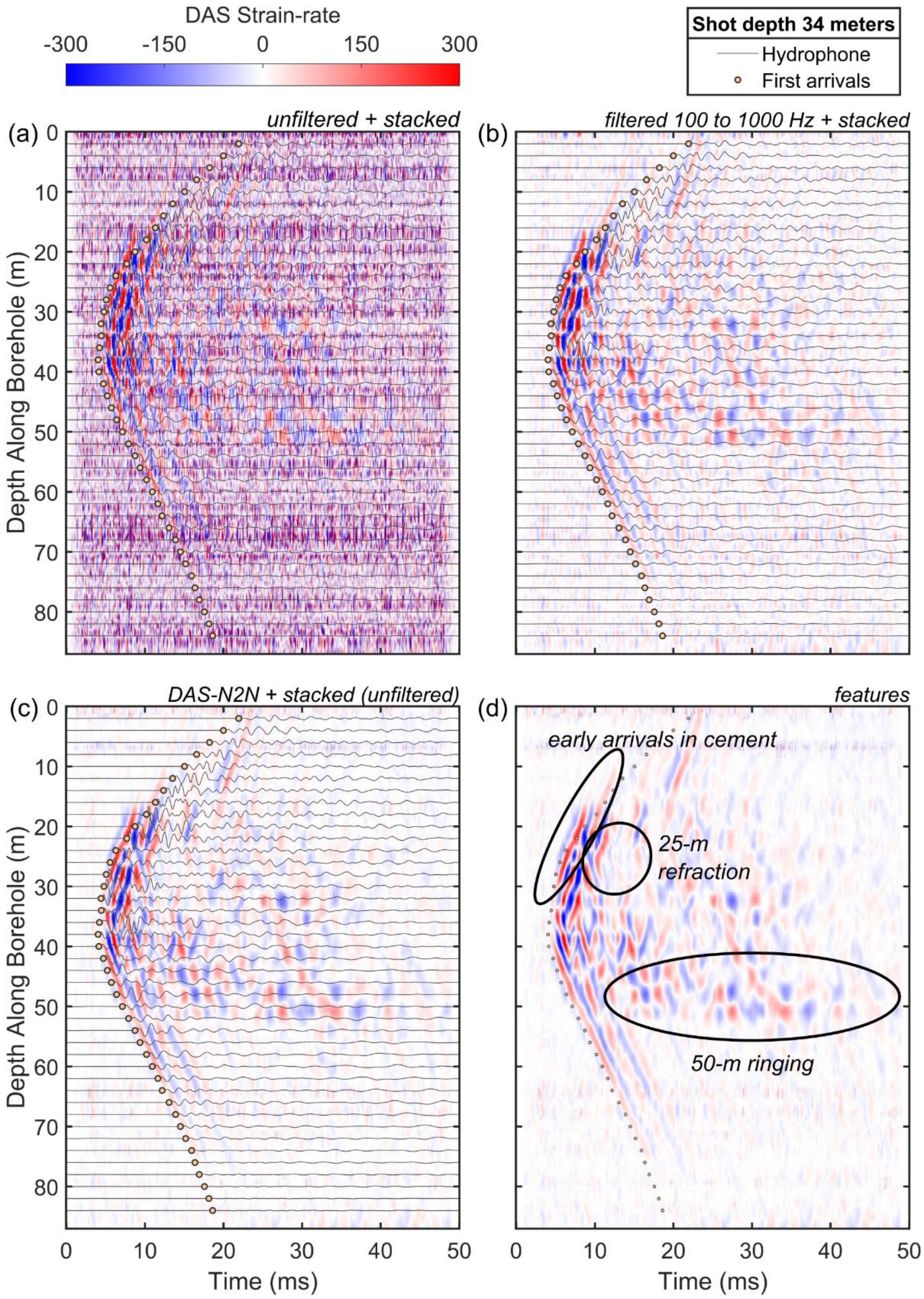

Figure 2. Stacked DAS and hydrophone traces for shot depth 34 m, showing the raw DAS in strain-rate (a), band-pass filtered DAS in strain-rate (b), and denoised DAS using the pre-trained DAS-N2N model (c). The hydrophone first-arrival picks are shown as circles. (d) DAS features highlighted on the DAS-N2N data. See Supporting Information Figures S2-S12 for all shot depths and example raw data before stacking.

We find several different interesting features in the denoised DAS shot-gathers, whose visibility varied slightly between the shot depths. For example, almost all shot depths reveal that at shallower depths, the DAS first arrivals overtake the hydrophone first arrivals. This indicates that the fiber-optic cable is probably more sensitive to the vibrations travelling through the cemented borehole rather than the subsurface medium at shallower depths. For the shot depth at 34 m, this is observed above 30 m (highlighted in Figure 2d), however for other shot depths this feature was observable down to 38 m depth (see Supporting Information Figures S2-S12). This is unsurprising, considering 38 m coincides with the intersection between the Quaternary Sediments and the Scottish Coal Measures sections and is a major change in seismic wave speeds and lithology from looser clay, sand, and gravel to denser sandstone and mudstone. The Quaternary Sediments likely have slower wave speeds than the cemented borehole. Thus, the first arrivals at channel depths < 38 m are likely originating from rays travelling through the Scottish Coal Measures and then refracting up the borehole. This transition was seen for all shot depths and highlights a limitation of using a cemented fiber-optic cable as a receiver if the surrounding seismic wave speeds are slower than the borehole material. Furthermore, the upgoing DAS signal is found to degrade quickly around 17 m for the deeper shot depths (≥ 30 m). This coincides with the bottom of the made-ground casing in borehole GGA05 extending down to 17.7 m (Barron et al., 2020), which consists of a permanent steel casing surrounded by 140 mm thick annulus grout (Supporting Information Figure S13). This highlights the importance of considering the borehole design when interpreting datasets, along with mitigating against these effects during construction and installation.

Another interesting feature made discernible through the denoising of the DAS data is the ringing observed at around 50 m depth (also highlighted in Figure 2d), which coincides with the Glasgow Upper Coal seam. This was mostly observable with the deeper shot depths. While the width of the ringing is likely an artifact of the 3-m gauge length used, the ringing could indicate the presence of a low-velocity layer such as intact or collapsed coal being surrounded by faster mudstone and sandstone layers. Similar strain amplifications in weakness and low-velocity zones have been previously observed in several larger-scaled DAS surveys (e.g., Jousset et al., 2018; Ma et al., 2024). The ringing is not observable in the hydrophone data due to the larger channel spacing, highlighting a strength in the DAS data. Furthermore, it is interesting that even though we are using a P-wave source located 10 m perpendicular to the fiber-optic cable orientation, which in theory should lead to negligible signal content at the trace apex due to the fiber-optic cable's insensitivity to perpendicular motion, the apex of the source signal is clear in the DAS data. This indicates that the first-arrival seismic waves are not arriving perpendicular to the cable but instead have refracted through a faster medium.

As a further comparison between the DAS and hydrophone data, we also compute the signal-to-noise ratio (S/N) in both time and frequency domain:

$$S/N_{time} = \frac{RMS_{signal}}{RMS_{noise}}, \qquad (1)$$

$$S/N_{freq} = \frac{PSD_{signal}}{PSD_{noise}}, \qquad (2)$$

where RMS is the root-mean-square and PSD is the power spectral density of the traces. S/N analysis in the time domain commonly uses time windows centered around the first arrival of a seismic wave (e.g., Correa et al., 2017) and can help indicate how discernible the first arrivals are at different depths and distances away from the source. Clear and accurate first arrivals are essential when inverting for seismic velocity structure using techniques such as crosswell or vertical seismic profile (VSP) tomography (e.g., Dillon and Collyer, 1985;

Harlan, 1990; Sabbione and Vellis, 2010), and thus prior knowledge about the expected first-arrival resolution at different depths using different types of receivers can help with the design of the borehole monitoring setup. S/N analysis in the frequency domain, on the other hand, uses a time window starting near the first arrival and covers most of the main signal, characterizing the decay in signal with increasing distance at different frequencies. Figure 3 shows examples of normalized traces from the DAS (including the different denoising approaches) and hydrophone arrays at a common shot depth and channel depth, along with the time window used for the time- and frequency-domain S/N examinations.

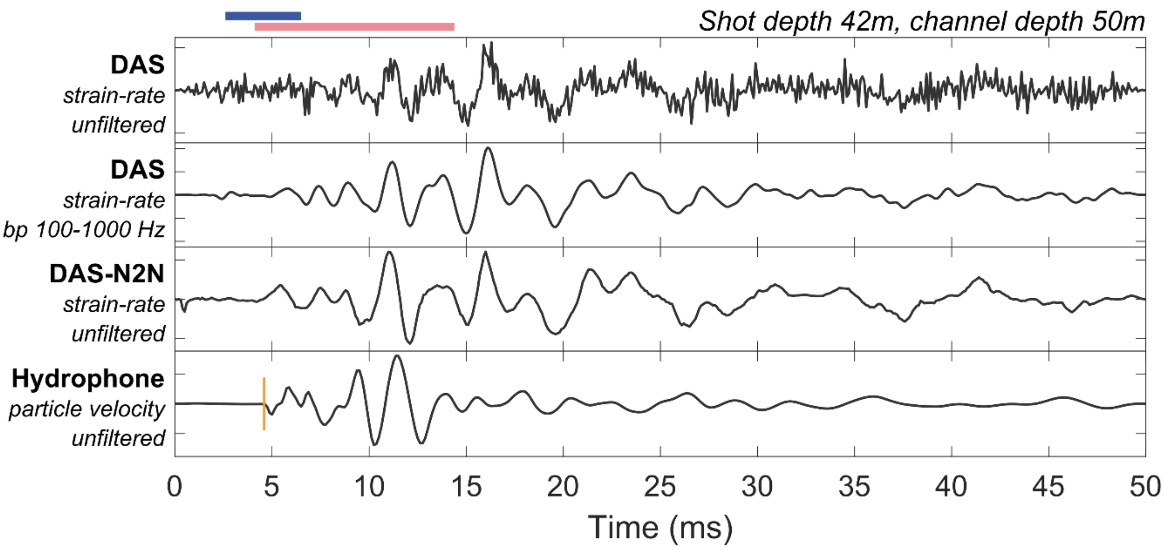

Figure 3. Normalized trace comparison between the DAS (top three rows) and the hydrophone (bottom) traces for shot depth at 42 m and a channel depth at 50 m. The unfiltered DAS trace is shown in the top row and the band-pass filtered DAS is shown in the second row. The third row shows the denoised DAS trace using the pre-trained DAS-N2N model. The time windows used for S/N analysis (Figure 4 and 5) are shown above the top row, where the shorter blue line (4 ms) is used for the time domain and the longer pink line (10 ms) is used for the frequency domain analysis. The manual first-arrival pick for the hydrophone is shown as a vertical orange line.

For all stacked traces with common channel-shot pairs available for both the hydrophone and DAS data, we compute the time-domain S/N using Equation (1) and a time window based on manual picks of the hydrophone first P-wave arrival. For each trace, the S/N is computed using a 4 ms signal time window centered on the hydrophone first arrival and 4 ms noise time windows extracted before the first arrival. If the first arrival occurs within 4 ms of the trace start, resulting in an overlap between the signal and noise time windows, we take the noise window from another shot depth using the same channel depth. The time-domain S/N results are shown in Figure 4 for the hydrophone data, the DAS data denoised using a 100-1000 Hz band-pass filter, and the DAS data denoised using the DAS-N2N model. As can be seen in Figure 4a, the hydrophone first arrivals are clear throughout the different shot-channel depth combinations (also seen in Figures 2 and 3), except for the very shallow channels during shot depths at 6 and 10 m, which coincides with the made ground and high attenuation levels. Commonly, a minimum S/N between 3-10 is required depending on the application. For the DAS data (Figures 4b and 4c), clear first arrivals can be found ± 20 to 30 m vertically from the shot depth, with a mean S/N of 3.8 and 6.2 for the band-pass filtered and DAS-N2N traces, respectively.

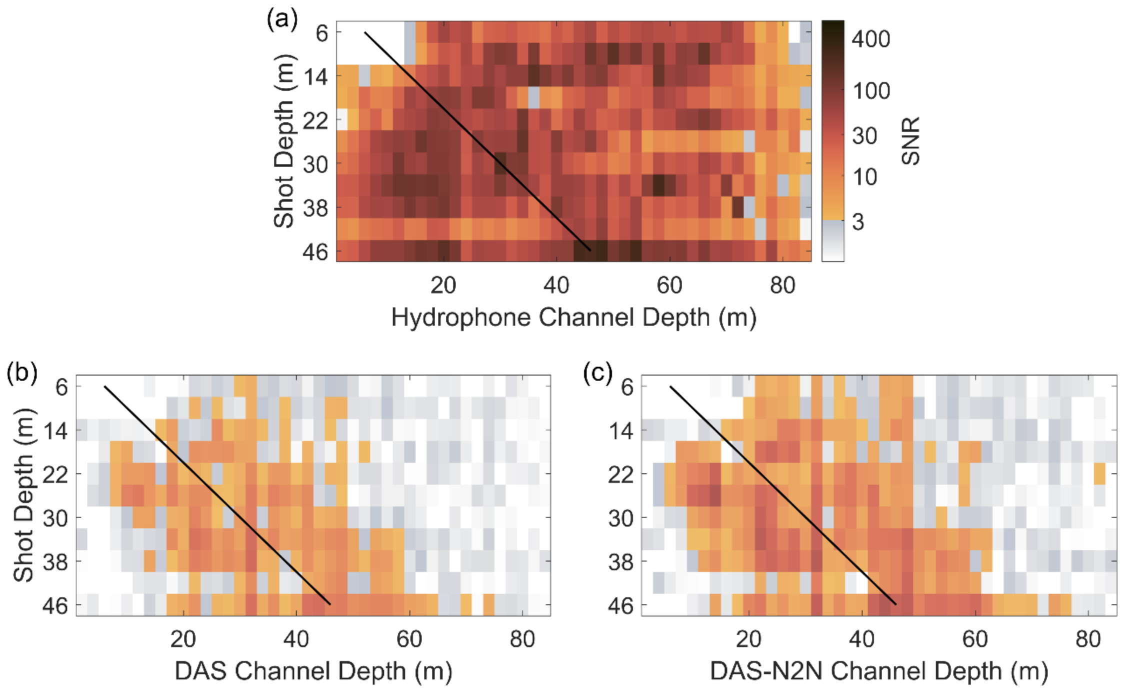

Figure 4. S/N in the time domain for the stacked (a) hydrophones, (b) DAS band-pass filtered between 100-1000 Hz, and (c) DAS denoised using DAS-N2N. The black solid line corresponds to equal shot and receiver depths. The signal time window (4 ms) used is shown in Figure 3 as the shorter blue horizontal line centered on the P-arrival.

Using the same traces as in the time-domain S/N evaluation, the S/N analysis in the frequency domain is estimated using Equation (2) and slightly longer time windows to gain insight into the attenuation at different frequencies. For the signal time window, we use a length of 10 ms starting 0.5 ms before the hydrophone first arrival. We use the same length for the noise window, extracting it from the beginning of the trace. Similar to the time-domain S/N calculation, if the noise and signal windows overlap we take the noise window from another shot depth but using the same channel depth. The S/N is then estimated using the PSD of the signal and noise time windows, computed using a multitaper technique (Prieto et al., 2009). The results are shown in Figure 5 for the hydrophone, DAS (unfiltered, raw strain-rate), and DAS-N2N denoised DAS. As can be seen in the hydrophone S/N, after travelling horizontally the 10 m between the boreholes (i.e., 0 m vertical distance), the source signal (originally 4 kHz) still has a high S/N along the frequency bandwidth and a peak frequency of 1.5 kHz. At larger vertical distances, the peak frequency decreases to between 0.5-1 kHz. The DAS data, on the other hand, display different frequency characteristics in its signal content. The low-frequency levels at small vertical distances are similar to the hydrophone data, while the high frequencies are heavily attenuated above 1 kHz for the shortest raypath distances. This loss of high frequency signal has been observed in similar studies and can be explained by strong damping with a soft rock environment (Butcher et al., 2021). While there may be an additional signal loss due to ghost frequencies caused by gauge length effects, the short 3m gauge length used in this study provides a good response over the frequency range of interest (Koedel et. al., 2024) and a similar signal loss is also present in the hydrophone data. Thus, considering the strong near-surface high-frequency attenuation and how our main recorded signal was found below 2 kHz, future surveys would be able to produce similar results by letting the interrogator downsample after recording to 2-4 kHz, saving valuable disk space at the same time. When comparing the raw and DAS-N2N denoised DAS data, at vertical distances greater than 30 m the S/N is less than 10 at all frequencies for both. At shorter vertical distances, however, the DAS-N2N model is able to enhance the signal significantly. For example, at 0 vertical distance (i.e., the rays recorded 10 m horizontally across from the shot), the S/N at 1 kHz is 350 for DAS-N2N and 26 for the raw DAS signal. Overall, neither of the DAS denoising approaches are able to enhance the first arrival arrivals sufficiently to make it comparable to the hydrophone data set.

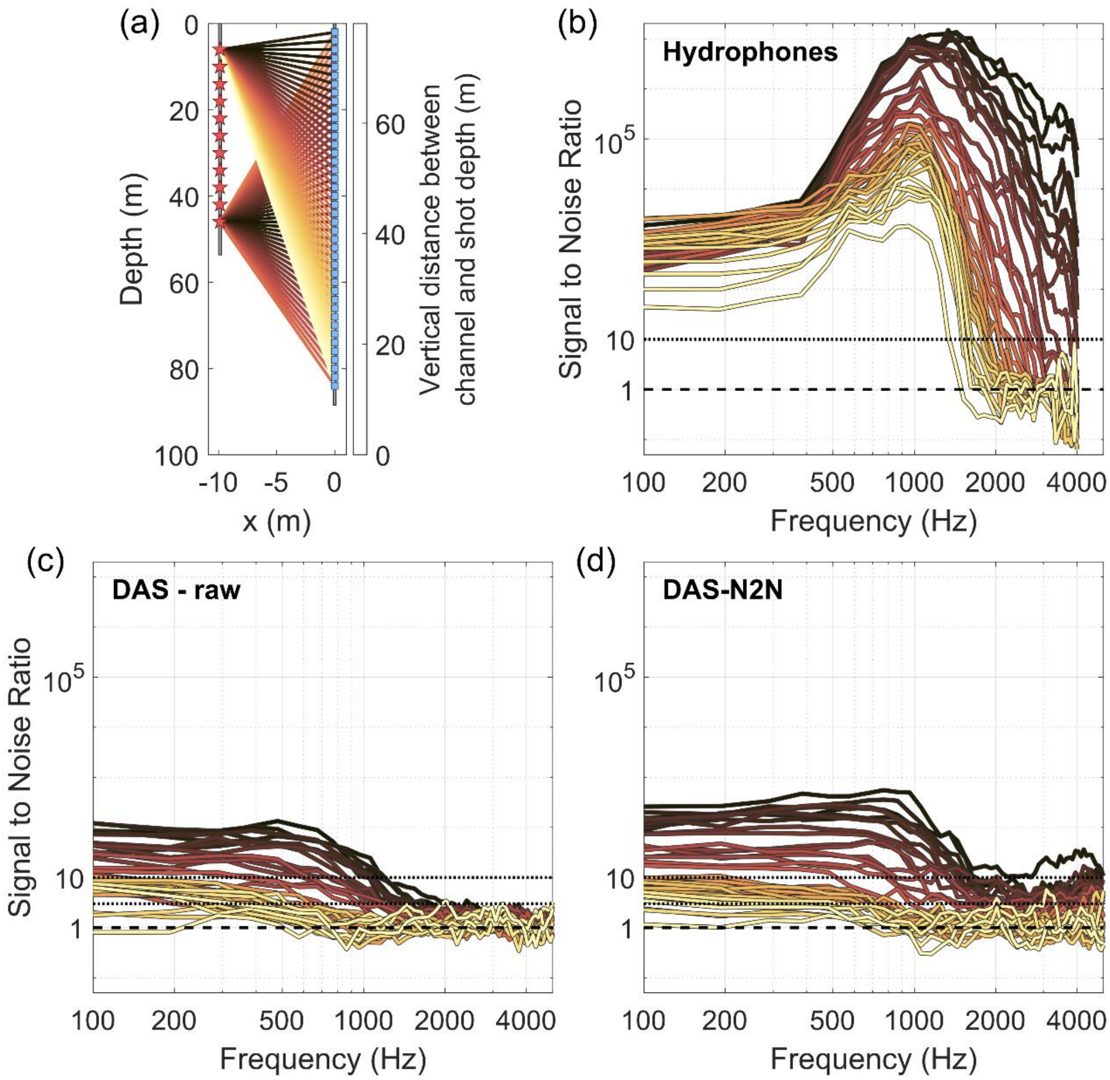

Figure 5. S/N in frequency domain. (a) Schematic view of trace coloring based on vertical distance travelled. Median S/N for selected vertical distance bins for stacked (b) raw hydrophone traces, (c) raw strain-rate DAS traces, and (d) DAS traces denoised using DAS-N2N. The signal time window (10 ms) used is shown in Figure 3 as the longer pink horizontal line starting just before the P-arrival. S/N = 1 and 10 are shown as black horizontal dashed lines.

Baseline Velocity Profile

At UKGEOS Glasgow, the seismic survey was completed before the heat pump installation, thus allowing us to obtain a baseline measurement of the seismic velocity structure. These measurements will provide an essential baseline against which future perturbations caused by heat production can be compared. Crosswell traveltime tomography is a powerful technique used to gain insight into the seismic velocity structure between two boreholes (e.g., Harlan, 1990; Zhang et al., 2012; Wuestefeld and Weinzierl, 2020). Here, we use the open-source pyGIMLi software (Rücker et al., 2017) to perform crosswell traveltime tomography using first arrivals from the hydrophone and DAS-N2N denoised DAS data. We manually pick first arrivals for all available combinations of source-receiver paths. For the hydrophone data set this provides 449 manual travel time picks, while the DAS produces 1843, with the difference corresponding to the higher spatial density of the DAS recordings. The low S/N of the DAS data, however, results in a lower ray-path coverage compared to the hydrophone data set. Based on the frequency content of the data sets, we select a 1 m cell size after considering the spatial resolution of the signal. This approach generates two broadly comparable velocity profiles, which we present in Figure 6 alongside the lithological information extracted from the rock chip logs.

Both profiles show P-wave velocities ranging between 1000 and 4500m/s, which generally increase with depth as the underlying geology transitions from poorly consolidated made ground to stiffer sandstone and mudstone units. While a distinct high velocity zone is observed between 40-50m, which coincides with the sandstone layer, the lower velocity coal seam layers are not clearly evident in the profile. The main evidence for coal present is the empty grid cells in the DAS data (Figure 6b) coinciding with the Glasgow Upper Coal at 50 m depth, which is still mostly intact but fractured (Monaghan et al., 2022). The lack of raypath coverage in these cells indicate low velocity and the rays preferred the faster paths around the low-velocity section. This lack of visible coal seams is partially due to the strong high-frequency attenuation, which lowers the dominant signal content to 1kHz from a source frequency of 4kHz, and results in vertical and horizontal resolution limits of 2-4m and 0.4-0.8m respectively. The thinner layers within the subsurface are therefore challenging to image and the velocity profile can be considered a smoothed representation of the subsurface.

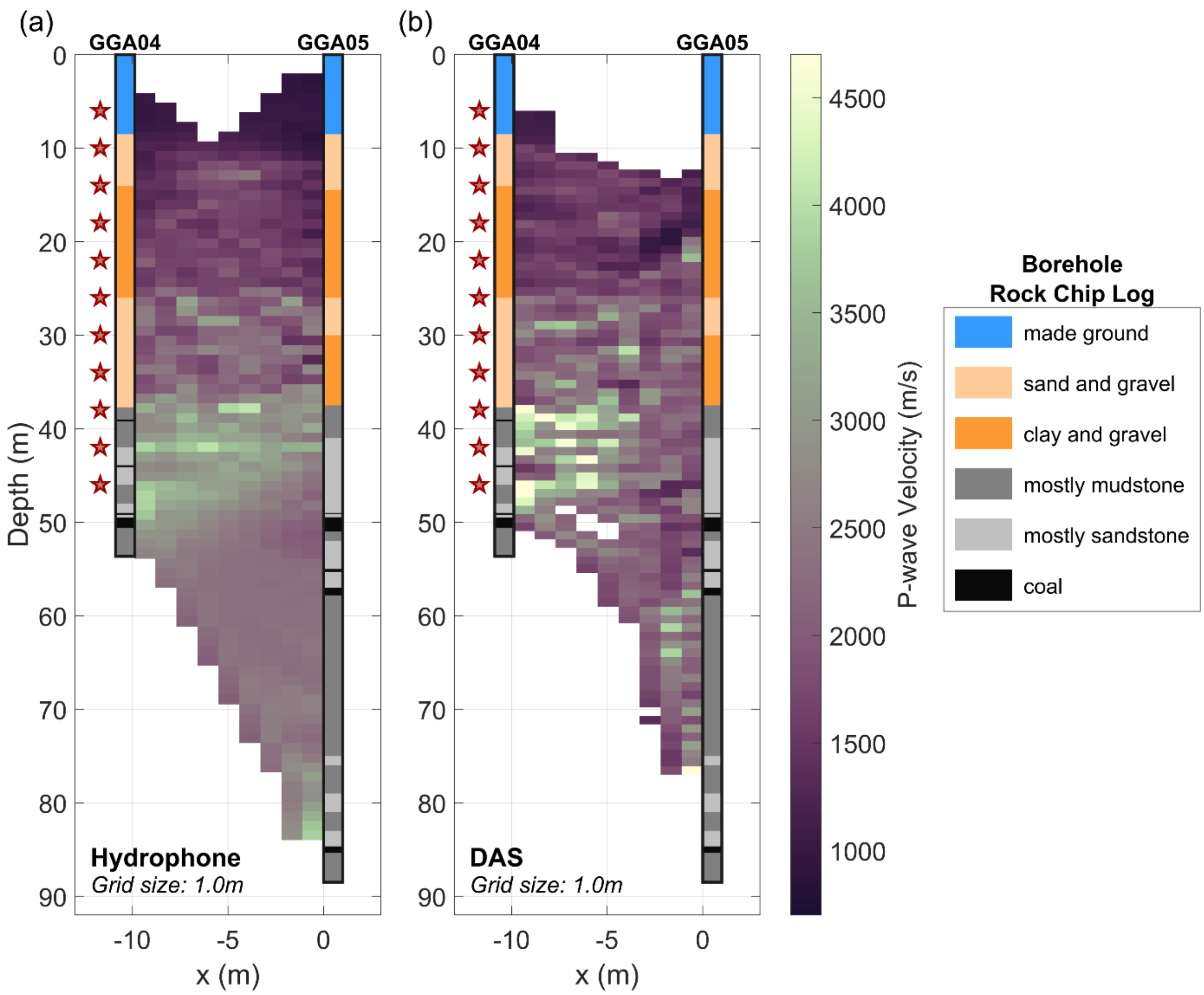

Figure 6. Crosswell traveltime tomography results using pyGIMLi (Rücker et al. 2017) and 1-m grids for the hydrophone (a) and DAS-N2N denoised DAS (b) data. The borehole rock chip logs are shown superimposed for comparison (Barron et al., 2020; Starcher et al., 2020). Note, borehole width is exaggerated. Shot depths are shown next to borehole GGA04 as stars.

De-coding the coda

Although identifying the onset of the first arrivals is challenging in the DAS data, the higher spatial resolution provided by the 0.25 m channel spacing allows identification of distinct arrivals within the coda of the signal. These features are not clearly identifiable in the hydrophone data due to a larger 2 m channel spacing. They can be used to characterize a higher degree of subsurface complexity than by using first arrivals alone, providing an opportunity to create higher-resolution sections which are able to identify thinner geological units that are below the resolution of the travel time tomography.

Considering the shot-gather from the source at 14 m (Figure 7a and Supporting Information Figures S4), we observe a relatively rich signal content after the first arrival, with multiple up- and down-going arrivals clearly imaged. We separate the upward (Figure 7b) and downward (Figure 7c) travelling wavefields through the addition and subtraction of normalized strain and velocity measurements. The velocity data set is created using transfer functions, which converts the strain to velocity measurements in the F-K domain following the approach of Daley et al. (2016) and Lindsey et al. (2020). Through this conversion, the polarity of the upward travelling arrivals is inverted, and therefore subtraction of the normalized strain and velocity measurements isolates the upward travelling arrivals, while addition separates the downward travelling wavefield. We find this approach more robust than the commonly adopted approach of separating wavefields in the F-K domain.

From the upward arrival plot (Figure 7c), we observe numerous linear wavefields that branch out from the first arrival, and we first determine the nature of these arrivals using an analytical approach. In Figure 8 we construct a simple geometry for a shot located at a depth of z_s and a receiver at z_r, which are positioned within boreholes separated by a distance x.

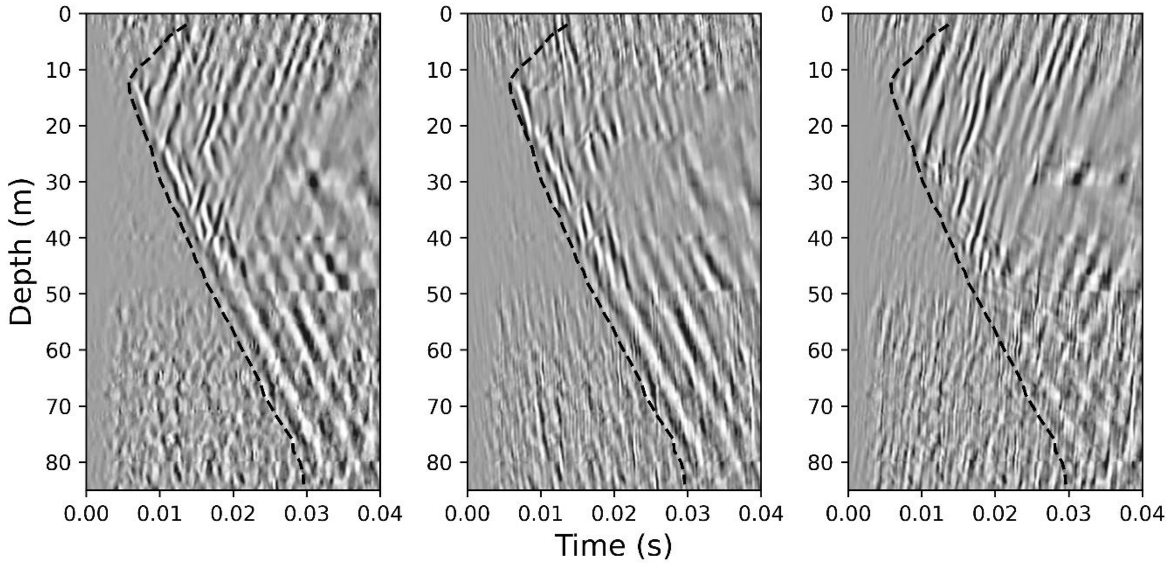

Figure 7. a) Shot-gather from a source located at 14 m with clear multiple arrival present in the later signal; b) Downward travelling arrivals created after adding the velocity from the strain measurements; c) Upward travelling arrivals after subtracting the strain and velocity measurements together. First arrivals identified from the hydrophone data set are shown by the black dashed line.

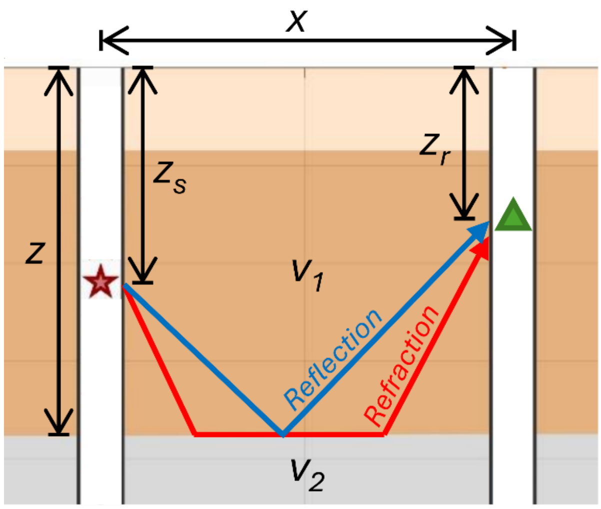

Figure 8. Schematic diagram illustrating the geometry used to model refracted (blue line) and reflected (red line) arrivals from a crosswell seismic survey.

Using this geometry, we model refracted and reflected arrivals from a boundary at the depth *z*, with a velocity v_1 above the boundary and v_2 below. For a refracted arrival the travel time (tt_{refrac}) is

$$tt_{refrac} = \frac{2z - z_s - z_r}{v_1 \cos(i_c)} + \frac{x - (2z - z_s - z_r)\tan(i_c)}{v_2}, \quad (3)$$

where i_c is the critical angle. The travel time for a reflected arrival (tt_{reflec}) can be expressed by

$$tt_{reflec} = \frac{(2z - z_s - z_r)}{v_1} \sqrt{1 + \frac{x^2}{2(2z - z_s - z_r)^2}} \quad (4)$$

following Stewart and Marchisio (1991). Using these equations, we model reflected and refracted arrivals recorded in shot-gathers from sources located at 14 m and 26 m (Figure 9). Both shot-gathers have prominent arrivals at these locations, and we model their travel times by constraining the P-wave velocity using the tomography results. For the 14 m shot-gather, we show the travel time for arrivals from a boundary at 25 m, where the P-wave velocity increases from 1650 m/s to 2000 m/s. With the 26 m shot-gather, we focus on a boundary at 39 m, where the tomography model shows a velocity increase from 2300 m/s to 2900 m/s. By overlaying these results on the shot-gathers, we conclude that the observed wavefield can only be refracted arrivals and not reflections. While the modelled refracted arrivals are in good agreement with the observed wavefields, the reflections display significantly different gradients and increasing the velocity to match the arrival results in unrealistic first arrival times.

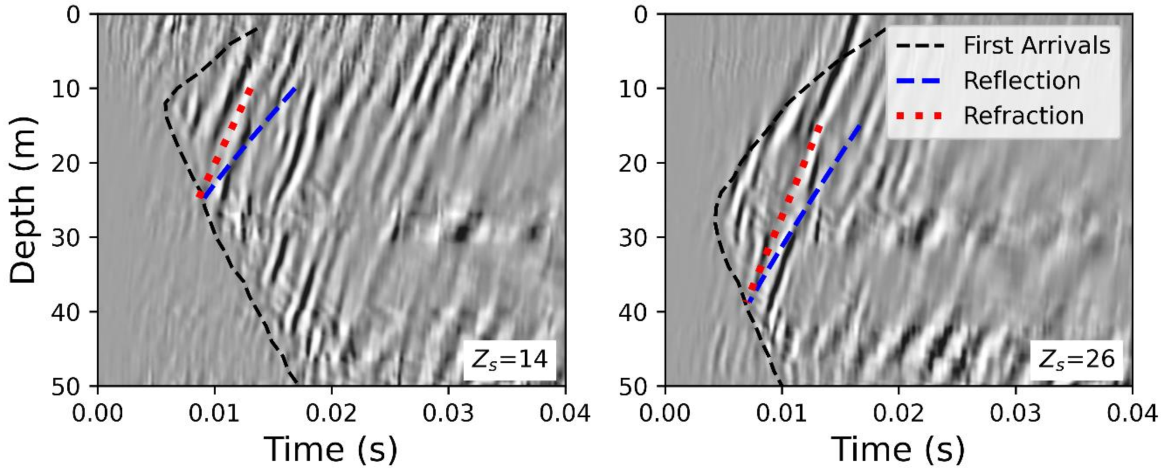

Figure 9. Upward travelling arrivals recorded from shot locations at 14 m (left) and 26 m (right) which are overlain by modelled reflected (blue dashed line) and refracted arrivals (red dotted line) for velocity boundaries at 25 m and 39 m depth respectively. When constraining the velocities using first arrival travel times (dashed black line), we show these are refracted arrivals.

As these are refracted arrivals, we use a linear stack to combine the separate shot-gathers after correcting for the time delay between shot locations. If these were instead reflections, we would need to apply a normal moveout correction ahead of stacking. We focus on the 25-50 m depth range, which has a number of prominent boundaries, and we select traces with shots above this horizon (i.e. 10, 14, 18 and 22 m). This ensures that refracted arrivals from the same interface are stacked and that near-source effects are avoided. We use the shot at 22 m as our reference shot-gather and cross-correlate it with the corresponding channels of the selected shot gathers. From these we calculate the median time correction for each shot-gather, which is then applied ahead of stacking the individual channels. We find that there is a very strong correlation between the traces, with a maximum standard error of 0.007 ms, which allows us to calculate a consistent time correction (Supporting Information Figure S14). The resulting stacked section is shown in Figure 10, and when compared to the individual shot gathers, there has been an improvement in the resolution and clarity of the main prominent arrivals within the region of interest.

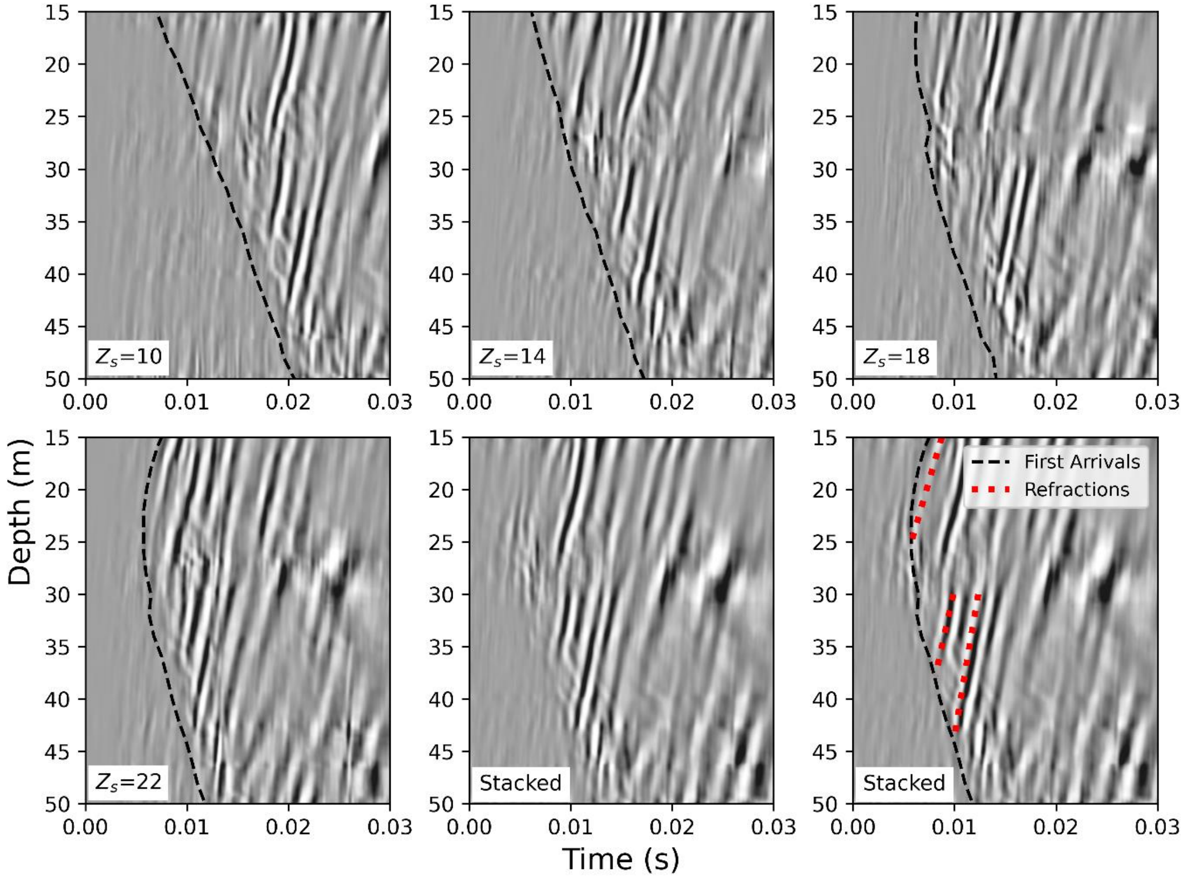

Figure 10. Individual shot-gathers from a source located at: a) Z_s=10 m; b) Z_s=14 m; c) Z_s=18 m; d) Z_s=22 m. e) Linear stack of the shot-gathers, demonstrating they are primarily refractions; f) modelled arrivals from a depth of 25, 38 and 44 m are displayed with red dashed lines. While the stacked section maintains the main features observed in the individual shot gathers, there is also an improvement in the resolution of arrivals, e.g. 25-30m.

After restructuring Equation (3) to make the refracted travel time at the receiver (tt_{zr}) a function of the first arrival for a given interface (tt_{z0}), we produce

$$tt_{zr} = tt_{z0} + \frac{z - z_r}{v_1 \cos(i_c)} - \frac{(z - z_r)\tan(i_c)}{v_2} \qquad (5)$$

for a simple two-layer case. Using this approach, we model the main prominent arrivals that are present in the stacked section. We constrain the depth of these boundaries using their intersection point with the first arrivals and base the initial velocity values on the tomography results. Using this approach, we determine that these arrivals originate from boundaries at depths of 25, 38 and 44 m, and represent velocity changes from 1650-1900 m/s, 2300-2700 m/s and 2800-3200 m/s respectively. The depths of these arrivals correlate well with the significant boundaries in the borehole log (Figure 11). We have therefore demonstrated that the ability of DAS recordings to identify refracted arrivals can provide more accurate imaging of the prominent subsurface boundaries than the tomographic results.

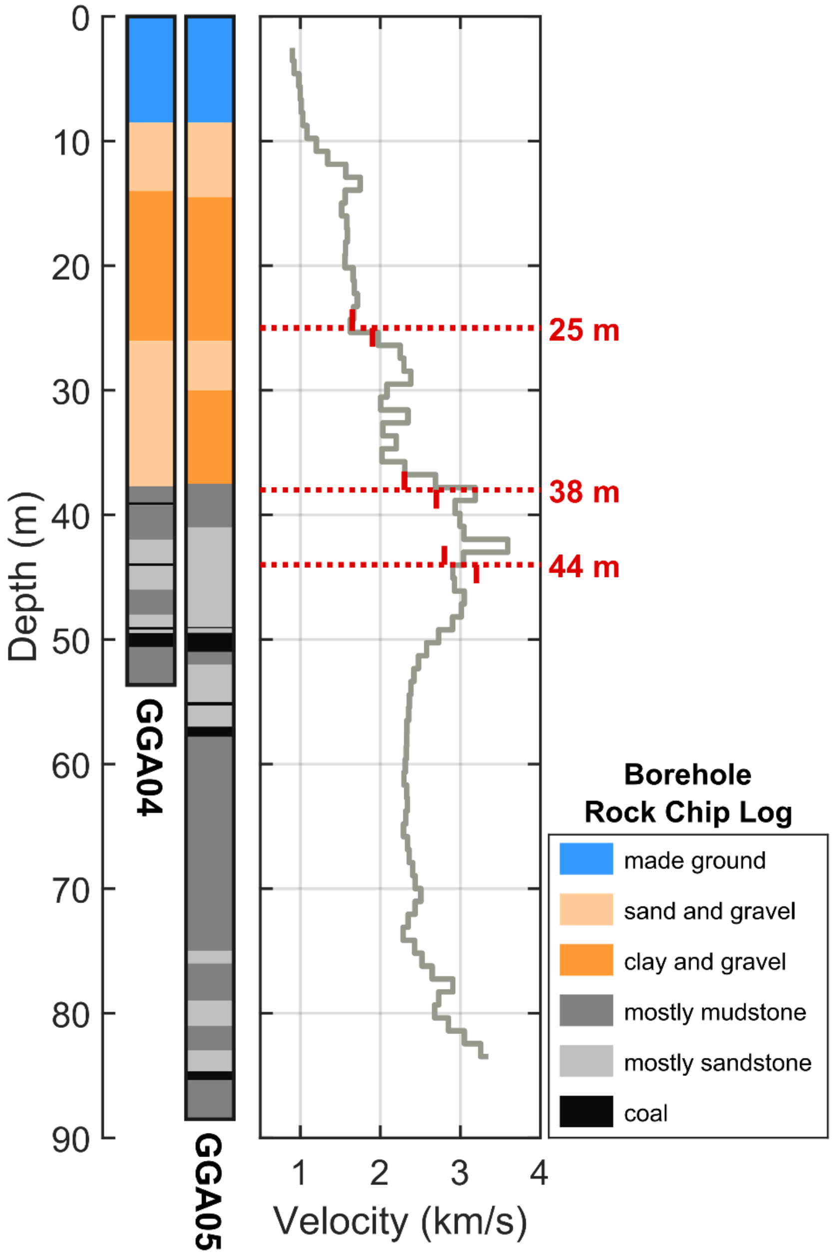

456

457 **Figure 11.** (left) Borehole log for source and receiver wells. (right) Tomographic section

458 produced from first arrivals and average velocity profile. Arrivals modelled in DAS coda

459 section are shown by red dashed lines.

460

Discussion

In our assessment of the suitability of using DAS in a shallow urban geothermal borehole setting, we find that the noise levels are significantly higher than the co-located hydrophone array. This is especially noticeable with the first arrivals, which is problematic for traveltime tomography. While the hydrophone array produces distinct first arrivals across the majority of the array (except the top 10 m coinciding with made ground), the noise levels and the sensitivity of the DAS array hinder clear first arrivals at vertical distances greater than 30 m between the shot and channel. This is likely partly due to using multimode fiber-optic cables designed for DTS instead of single-mode cables designed for DAS (e.g., Koedel et al., 2024). A simple approach to improving S/N could be to increase the number of shots at each source depth, however this alone is unable to overcome the relative insensitivity of the DAS array to direct P-waves that arrive at a near-normal incident angle. Newly developed SV-wave sparker sources offer the potential to produce signals that arrive at more favorable incident angles (Koedel et al., 2024) and may prove to be a more optimum source for crosswell DAS surveys.

In this study, we find that the pretrained DAS-N2N model (Lapins et al., 2024) was most effective at suppressing the background noise across a broad range of frequencies of the DAS data. It is worth highlighting that we have applied an early iteration of the model, which has only been trained on a fiber-optic cable deployed on the surface of Antarctica. While it performed surprisingly well considering that a shallow borehole in an urban setting is different to the quiet setting of Antarctica, further developments of the model using UKGEOS data or similar sites could significantly improve the performance of this method.

In both the DAS and hydrophone data sets, there is a significant loss of high-frequency signal due to the strong damping of the soft rock environment. In our survey configuration, we used a 4 kHz source and therefore adopted a 10 kHz DAS sampling rate, which created significant data volumes when also combined with the 0.25 m channel spacing. However, for even the shortest travel path distances (10 m), the main signal frequency was between 1-2 kHz. Thus, for interrogators with the option to downsample after recording the signal, future similar surveys can save significant disk space by downsampling to around 2-4 kHz instead.

Within the immediate near surface, we observe that the first arrivals recorded by the DAS array are clearly influenced by the borehole design, with much higher apparent velocities observed than those captured by the hydrophone array. This is likely due to the DAS array being more sensitive to P-waves travelling through the high-velocity borehole casing than the lower velocity sediments and made ground. At UKGEOS, the boreholes include two 3-cm thick permanent steel casings within the cement, which for the receiver borehole GGA05 extend down to 17.7 m and 40.5 m depth, respectively (Barron et al., 2020) (Supporting Information Figure S13). The deeper 40.5 m casing coincides with the 38-m deep boundary between the Quaternary Sediments and the deeper Scottish Coal Measures (where average P-wave velocity increases from ~2000 m/s to ~3000 m/s, see Figure 11). Considering the high P-wave velocity of steel (6100 m/s, e.g., Tendürüs et al., 2010), any waves travelling through the casing would be significantly faster than the surrounding medium consisting of sand, gravel, and clay. This is further compounded by the fiber being most sensitive to particle motion travelling in the direction of the array, such as P-waves travelling along the borehole casing. Thus, this results in a degree of ambiguity when relying on first arrivals alone to produce a velocity model and highlights a clear limitation of using cemented fiber-optic cables at shallow depths for DAS purposes. Furthermore, Gurevich et al. (2023) modelled how borehole design affects DAS amplitudes using a P-wave source ~1 km away from the receivers and found that while cement can lower the DAS amplitude by up to 2%, introducing a 1-cm steel casing increases this effect up to 5%. While no such effect is visible for the deeper steel casing at UKGEOS, the 17.7-m deep, 3-cm thick steel casing coincides with a rapid decay in the DAS signal observed for the deeper shot depths (see Figure 2 and Supporting Information Figures S7-S12), highlighting another limitation to be considered. However, we observe neither of these borehole effects near the coal seams, which are the main area of monitoring interest, due to their greater depths.

Instead of working solely with the first arrivals, which are associated with many limitations in an urban shallow setting as shown in this study, our analysis highlights the advantage of DAS' unparalleled spatial resolution. We observe clear refracted arrivals within the shot gathers, which are captured in much greater detail than by the hydrophone array due to the higher spatial resolution and sensitivity patterns of DAS. These refracted arrivals provide the opportunity to identify discrete layers within the subsurface which are unresolvable when relying on first arrivals alone. Furthermore, they also provide reference images that can be used to detect seismic velocity and amplitude changes caused by variations in subsurface properties over time. While further developments in modelling are required to fully exploit the information that these arrivals provide, this study shows that DAS is capable of providing higher resolution data sets than using classical traveltime tomography methods.

Alongside refracted arrivals, we also detect localized strain amplification at 50 m depth in the DAS data, which is not seen in the hydrophone data (Figure 2). This coincides with the Glasgow Upper Coal seam, which consists of mainly intact and collapsed coal with fractures from nearby workings (Monaghan et al., 2022). These types of local strain amplifications have also been observed in several other DAS studies which conclude that they are caused by trapped waves within low-velocity layers (e.g., Jousset et al., 2018; Ma et al., 2024). Here, we also consider that the ringing feature is likely produced by reverberating seismic waves caused by the strong impedance contrast between the coal seam and the surrounding mudstone and sandstone layers. Finite-difference methods could be used to model the low-velocity layers (Rodríguez-Pradilla and Eaton, 2018), providing an additional approach to image and monitor coal seams using DAS.

Finally, baseline geophysical measurements are vital for the future characterization of subsurface impact of water circulation over time in an abandoned mine (e.g., Furre et al., 2017). They allow for direct comparison to any future repeated surveys and provide insight into the initial state of the mine. At UKGEOS Glasgow, we were able to complete the seismic survey prior to heat pump installation, thus allowing us to obtain a baseline measurement of the seismic velocity structure between the two boreholes. Future surveys as the system is perturbed by heat extraction could identify temporal changes in seismic velocity produced by, for example, changes in temperature, changes in fluid saturation, or geomechanical processes such as the opening of fracture networks or the formation of voids. Wuestefeld and Weinzierl (2020) compared borehole spacing configurations for optimal DAS crosswell seismics at the Svelvik CO_2 storage in Norway, finding that shorter distances between boreholes (10-20 m) were ideal to detect travel-time differences between surveys. Thus, differences in travel-times between surveys can reveal regions affected by the geothermal operations. Furthermore, as the fiber-optic cables are permanently installed in the UKGEOS boreholes, identical surveys can be easily repeated without the need to sacrifice the use of these boreholes. In contrast, the installation of hydrophone arrays would require either the sacrificing of the wells for any other use, or the repeated insertion and removal of the geophysical instruments for each survey.

Conclusions

In our assessment of DAS for crosswell imaging of a shallow, urban, mine water geothermal site, we find that the DAS data have higher noise levels and are more sensitive to the borehole construction compared to conventional instruments, which affect first arrivals and limits traveltime analysis. However, as more DAS-appropriate sources and machine-learning-based denoising methods are developed and locally adapted to shallow geothermal sites, the signal strength in DAS data will improve significantly. Furthermore, we find that DAS' higher spatial resolution provides invaluable insight into the subsurface; low-velocity layers such as coal seams cause local channel amplification of strain, and the ability to discern refracted phases allow for identification of discrete layers within the subsurface.

Installing fiber-optic cables alongside mine water boreholes can therefore provide a cost-effective approach to monitor any subsurface changes in shallow geothermal projects and remove the requirement to drill additional nearby monitoring wells. The semi-permanent nature of the installed fiber also lends itself to long-term ongoing monitoring and recording of repeatable data sets. Through our analysis, we find that DAS can potentially provide a powerful method to monitor geothermal sites in urban settings, which we illustrate by producing a baseline measurement of the UKGEOS mine prior to heat pump installation

Acknowledgements

We would like to thank three anonymous reviewers for their constructive feedback which helped improve this article. Additionally, we thank Kyle Walker-Verkuil, Rumen Karaulanov, Athena Chalari, Pierpaolo Marchesini, Anna Stork, Filipe Valentim, Matt Guy, Ophelia George, Luke Wedmore, and Joe Asplet for their help with the fieldwork preparation and in the field. This work was supported by the Natural Environment Research Council (NERC) (NE/R017492/1, "UKSGL"; NE/R017956/1, "EQUIPT4RISK"; NE/R018006/1, "SHAPE-UK") and the Bristol and Oxford Passive Seismic Research Consortium ("BOPS"). The contributions of J. E. Chambers and V. Starcher to this paper are published with the permission of the Executive Director of the British Geological Survey (NERC). This work was supported by the British Geological Survey via NERC national capability.

Data Availability Statement

The dataset used in this study is publicly available through the British Geological Survey National Geoscience Data Centre (NGDC) (https://webapps.bgs.ac.uk/services/ngdc/accessions/index.html#item177047). The dataset contains the active DAS and hydrophone survey on January 31st to February 2nd 2022. Additionally, it contains passive DAS recording of the background noise during the night between February 1st to 2nd, using the same parameters as the active survey but with a sampling rate of 2 kHz.

References

Adams, C., A. Monaghan, and J. Gluyas, 2019, Mining for heat: Geoscientist, **29**(4), 10-15. https://doi.org/10.1144/geosci2019-021

Baird, A. F., A. L. Stork, S. A. Horne, G. Naldrett, J. M. Kendall, J. Wookey, J. P. Verdon, and A. Clarke, 2020, Characteristics of microseismic data recorded by distributed acoustic sensing systems in anisotropic media: Geophysics, **85**(4), KS139-KS147. https://doi.org/10.1190/geo2019-0776.1

Barron, H. F., V. Starcher, A. A. Monaghan, K. M. Shorter, and K. Walker-Verkuil, 2020, Mine water characterisation and monitoring borehole GGA05, UK Geoenergy Observatory, Glasgow. British Geological Survey Open Report, OR/20/025. https://doi.org/10.5285/714fe9fc-ce77-4479-8053-1c5fd4e86f06

Butcher, A., A. L. Stork, J. P. Verdon, J. M. Kendall, K. Plenkers, F. Booth, M. Boneham, and A. Koe, 2021, Evaluating rock mass disturbance within open-pit excavations using seismic methods: A case study from the Hinkley Point C nuclear power station: Journal of Rock Mechanics and Geotechnical Engineering, **13**(3), 500-512. https://doi.org/10.1016/j.jrmge.2020.12.001

Correa, J., A. Egorov, K. Tertyshnikov, A. Bona, R. Pevzner, T. Dean, B. Freifeld, and S. Marshall, 2017, Analysis of signal to noise and directivity characteristics of DAS VSP at near and far offsets—A CO2CRC Otway Project data example: The Leading Edge, **36**(12), 994a1-994a7. https://doi.org/10.1190/tle36120994a1.1

Daley, T. M., D. E. Miller, K. Dodds, P. Cook, and B. M. Freifeld, 2016, Field testing of modular borehole monitoring with simultaneous distributed acoustic sensing and geophone vertical seismic profiles at Citronelle, Alabama: Geophysical Prospecting, **64**(5), 1318-1334. https://doi.org/10.1111/1365-2478.12324

Dillon, P. B., and V. A. Collyer, 1985, On timing the VSP first arrival: Geophysical Prospecting, **33**(8), 1174-1194. https://doi.org/10.1111/j.1365-2478.1985.tb01358.x

Dobson, P., E. Gasperikova, Y. Zhang, G. Mosey, A. Kolker, X. Liu, and Y. Polsky, 2023, US DOE Clean Energy Demonstration Program on Current and Former Mine Land – A

Review of Geothermal Energy Case Studies and Opportunities: Proceedings of the 48th Workshop on Geothermal Reservoir Engineering, Stanford University, SGP-TR-224. https://www.osti.gov/servlets/purl/1959586 [last accessed August 7, 2024]

Farr, G., J. Busby, L. Wyatt, J. Crooks, D. I. Schofield, and A. Holden, 2021, The temperature of Britain's coalfields: Quarterly Journal of Engineering Geology and Hydrogeology, **54**(3), qjegh2020-109. https://doi.org/10.1144/qjegh2020-109

Furre, A. K., O. Eiken, H. Alnes, J. N. Vevatne, and A. F. Kiær, 2017, 20 Years of Monitoring CO2-injection at Sleipner: Energy procedia, **114**, 3916-3926. https://doi.org/10.1016/j.egypro.2017.03.1523

Gurevich, B., K. Tertyshnikov, A. Bóna, E. Sidenko, P. Shashkin, S. Yavuz, and R. Pevzner, 2023. The effect of the method of downhole deployment on distributed acoustic sensor measurements: Field experiments and numerical simulations: Sensors, **23**(17), p.7501. https://doi.org/10.3390/s23177501

Hall, A., J. A. Scott, and H. Shang, 2011, Geothermal energy recovery from underground mines: Renewable and Sustainable Energy Reviews, **15**(2), 916-924. https://doi.org/10.1016/j.rser.2010.11.007

Harlan, W. S., 1990, Tomographic estimation of shear velocities from shallow cross-well seismic data: SEG Technical Program Expanded Abstracts 1990, 86-89. https://library.seg.org/doi/pdf/10.1190/1.1890369 [last accessed August 7, 2024]

Hudson, T. S., A. F. Baird, J. M. Kendall, S. K. Kufner, A. M. Brisbourne, A. M. Smith, A. Butcher, A. Chalari, and A. Clarke, 2021, Distributed acoustic sensing (DAS) for natural microseismicity studies: A case study from Antarctica: Journal of Geophysical Research: Solid Earth, **126**(7), e2020JB021493. https://doi.org/10.1029/2020JB021493

Jousset, P., T. Reinsch, T. Ryberg, H. Blanck, A. Clarke, R. Aghayev, G. P. Hersier, J. Hennings, M. Weber, and C. M. Krawczyk, 2018, Dynamic strain determination using fibre-optic cables allows imaging of seismological and structural features: Nature communications, **9**(1), 2509. DOI: 10.1038/s41467-018-04860-y

Koedel, U., A. L. Stork, A. David, and T. Fechner, 2024, Evaluating distributed acoustic sensing for crosswell seismic surveys with helical and linear fibers using conventional P-, SH-, and SV-wave sources: The Leading Edge, **43**(11), 726-734. https://doi.org/10.1190/tle43110726.1

Lapins, S., A. Butcher, J. M. Kendall, T. S. Hudson, A. L. Stork, M. J. Werner, J. Gunning, and A. M. Brisbourne, 2024, DAS-N2N: machine learning distributed acoustic sensing (DAS) signal denoising without clean data: Geophysical Journal International, **236**(2), 1026-1041. https://doi.org/10.1093/gji/ggad460

Lellouch, A., N. J. Lindsey, W. L. Ellsworth, and B. L. Biondi, 2020, Comparison between distributed acoustic sensing and geophones: Downhole microseismic monitoring of the FORGE geothermal experiment: Seismological Society of America, **91**(6), 3256-3268. https://doi.org/10.1785/0220200149

Lellouch, A., and B. L. Biondi, 2021, Seismic applications of downhole DAS: Sensors, **21**(9), 2897. https://doi.org/10.3390/s21092897

Lindsey, N. J., H. Rademacher, and J. B. Ajo-Franklin, 2020, On the broadband instrument response of fiber-optic DAS arrays: Journal of Geophysical Research: Solid Earth, **125**(2), e2019JB018145. https://doi.org/10.1029/2019JB018145

Ma, K. F., S. von Specht, L. W. Kuo, H. H. Huang, C. R. Lin, C. J. Lin, C. S. Ku, E. S. Wu, C. Y. Wang, W. Y. Chang. and P. Jousset, 2024, Broad-band strain amplification in an asymmetric fault zone observed from borehole optical fiber and core: Communications Earth & Environment, **5**(1), 402. https://doi.org/10.1038/s43247-024-01558-6

Monaghan, A. A., V. Starcher, H. F. Barron, K. Shorter, K. Walker-Verkuil, J. Elsome, T. Kearsey, S. Arkley, S. Hannis, and E. Callaghan, 2022, Drilling into mines for heat:

geological synthesis of the UK Geoenergy Observatory in Glasgow and implications for mine water heat resources: Quarterly Journal of Engineering Geology and Hydrogeology, **55**(1), qjegh2021-033. https://doi.org/10.1144/qjegh2021-033

Prieto, G. A., R. L. Parker, and F. L. Vernon III, 2009, A Fortran 90 library for multitaper spectrum analysis: Computers & Geosciences, **35**(8), 1701-1710. https://doi.org/10.1016/j.cageo.2008.06.007

Rücker, C., T. Günther, and F. M. Wagner, 2017, pyGIMLi: An open-source library for modelling and inversion in geophysics: Computers and Geosciences, **109**, 106-123, doi: 10.1016/j.cageo.2017.07.011.

Rodríguez-Pradilla, G., and D. W. Eaton, 2018, Finite-differences modelling of microseismicity associated with a hydraulic-fracturing stimulation in a coalbed methane reservoir: First Break, **36**(4), 41-48. https://doi.org/10.3997/1365-2397.n0081

Sabbione, J. I., and D. Velis, 2010, Automatic first-breaks picking: New strategies and algorithms: Geophysics, **75**(4), V67-V76. https://doi.org/10.1190/1.3463703

Shao, D., T. Li, L. Han, and Y. Li, 2022, Noise suppression of distributed acoustic sensing vertical seismic profile data based on time–frequency analysis: Acta Geophysica, **70**(4), 1539-1549. https://doi.org/10.1007/s11600-022-00820-9

Starcher, V., H. F. Barron, A. A. Monaghan, K. M. Shorter, and K. Walker-Verkuil, 2020, Mine water characterisation and monitoring borehole GGA04, UK Geoenergy Observatory, Glasgow. British Geological Survey Open Report, OR/20/024. https://doi.org/10.5285/83ab3481-45d9-475d-8814-008edc9fb1cb

Stewart, R. R., and G. Marchisio, 1991, Cross-well seismic imaging using reflections: SEG Technical Program Expanded Abstracts 1991, 375-378. https://doi.org/10.1190/1.1888915

Tendürüs, M., G. J. van Wijngaarden, H. Kars, M. Sintubin, I. S. Stewart, T. M. Niemi, and E. Altunel, 2010, Long-term effect of seismic activities on archaeological remains: A test study from Zakynthos, Greece: Ancient Earthquakes: Geological Society of America Special Paper, **471**, 145–156, doi:10.1130/2010.2471(13)

Tourei, A., E. R. Martin, A. T. Ankamah, J. A. Hole, and D. J. A. Chambers, 2024, An autoencoder-based deep learning model for enhancing noise characterization and microseismic event detection in underground longwall coal mines using distributed acoustic sensing monitoring: paper presented at the 58th U.S. Rock Mechanics/Geomechanics Symposium, Golden, Colorado, ARMA-2024-0207. https://doi.org/10.56952/ARMA-2024-0207

Verdon, J. P., S. A. Horne, A. Clarke, A. L. Stork, A. F. Baird, and J. M. Kendall, 2020, Microseismic monitoring using a fiber-optic distributed acoustic sensor array: Geophysics: **85**(3), KS89-KS99. https://doi.org/10.1190/geo2019-0752.1

Verhoeven, R., E. Willems, V. Harcouët-Menou, E. De Boever, L. Hiddes, P. Op't Veld, and E. Demollin, 2014, Minewater 2.0 project in Heerlen the Netherlands: transformation of a geothermal mine water pilot project into a full scale hybrid sustainable energy infrastructure for heating and cooling: Energy Procedia, **46**, 58-67. https://doi.org/10.1016/j.egypro.2014.01.158

Watson, S. M., R. Westaway, and N. M. Burnside, 2019, Digging deeper: The influence of historical mining on Glasgow's subsurface thermal state to inform geothermal research: Scottish Journal of Geology, **55**(2), 107-123. https://doi.org/10.1144/sjg2019-012

Wuestefeld, A., and W. Weinzierl, 2020, Design considerations for using Distributed Acoustic Sensing for cross-well seismics: A case study for CO2 storage: Geophysical Prospecting, **68**(6), 1893-1905. https://doi.org/10.1111/1365-2478.12965

Zhang, F., C. Juhlin, C. Cosma, A. Tryggvason, and R. G. Pratt, 2012, Cross-well seismic waveform tomography for monitoring CO2 injection: a case study from the Ketzin Site, Germany: Geophysical Journal International, **189**(1), 629-646. https://doi.org/10.1111/j.1365-246X.2012.05375.x